



Constraints on dynamic topography from asymmetric subsidence of the mid-ocean ridges

C. Evan Watkins^{a,c}, Clinton P. Conrad^{b,c,*}

^a Department of Earth and Planetary Sciences, Rutgers University, Piscataway, NJ, USA

^b Centre for Earth Evolution and Dynamics (CEED), University of Oslo, Oslo, Norway

^c Department of Geology and Geophysics, University of Hawaii at Manoa, Honolulu, HI, USA

ARTICLE INFO

Article history:

Received 4 July 2017

Received in revised form 5 December 2017

Accepted 8 December 2017

Available online xxx

Editor: B. Buffett

Keywords:

bathymetry

dynamic topography

seafloor subsidence

mid-ocean ridges

mantle flow

ABSTRACT

Stresses from mantle convection deflect Earth's surface vertically, producing dynamic topography that is important for continental dynamics and sea-level change but difficult to observe due to overprinting by isostatic topography. For long wavelengths ($\sim 10^4$ km), the amplitude of dynamic topography is particularly uncertain, with mantle flow models typically suggesting larger amplitudes (> 1000 m) than direct observations. Here we develop a new constraint on the amplitude of long-wavelength dynamic topography by examining asymmetries in seafloor bathymetry across mid-ocean ridges. We compare bathymetric profiles across the Mid-Atlantic Ridge (MAR) and the East Pacific Rise (EPR) and we find that the South American flank of both ridges subsides faster than its opposing flank. This pattern is consistent with dynamic subsidence across South America, supported by downwelling in the lower mantle. To constrain the amplitude of dynamic topography, we compare bathymetric profiles across both ridges after correcting bathymetry for several different models of dynamic topography with varying amplitudes and spatial patterns. We find that long-wavelength dynamic topography with an amplitude of only ~ 500 m explains the observed asymmetry of the MAR. A similar model can explain EPR asymmetry but is complicated by additional asymmetrical topography associated with tectonic, crustal thickness, and/or asthenospheric temperature asymmetries across the EPR. After removing 500 m of dynamic topography, both the MAR and EPR exhibit a slower seafloor subsidence rate ($\sim 280\text{--}290$ m/Myr^{1/2}) than previously reported. Our finding of only ~ 500 m of long-wavelength dynamic topography may indicate the importance of thermochemical convection and/or large viscosity variations for lower mantle dynamics.

© 2017 Elsevier B.V. All rights reserved.

1. Introduction

Convective flow in the mantle supports deflections of Earth's solid surface known as dynamic topography (e.g., Hager et al., 1985). Changes in this dynamic topography, which result from the time-dependence of mantle flow, have been identified as exerting important controls on sea level change (e.g., Conrad and Husson, 2009; Spasojevic and Gurnis, 2012) and continental dynamics (e.g., Liu, 2015) over timescales of millions of years. However, our understanding of the influence of dynamic topography is complicated by significant uncertainties over its amplitude. In particular, constraints on the long wavelength ($\sim 10^4$ km in width) components of dynamic topography range from a few hundred meters based on observational studies (e.g., Hoggard et al., 2016, 2017;

Molnar et al., 2015) to upwards of one kilometer from mantle flow models (e.g., Conrad and Husson, 2009; Flament et al., 2013; Hager et al., 1985; Spasojevic and Gurnis, 2012). To constrain this uncertainty, we look for the signature of dynamic topography within bathymetric observations of seafloor subsidence away from mid-ocean ridges (e.g., Zhong et al., 2007).

Numerical mantle flow models predict vertical stresses that support dynamic topography at the Earth's surface. Models based on tomographic constraints on mantle density heterogeneity depend on the conversion factor $R = \delta \ln(\rho) / \delta \ln(v_s)$, which translates a tomographically-constrained seismic velocity anomaly into a mantle density anomaly. Typical estimates of R range from 0.15 to 0.4, with uncertainty associated with the relationships between the thermal expansion coefficient, temperature, density, pressure, and composition (e.g., Gurnis et al., 2000; Karato and Karki, 2001). Previous studies have utilized a nearly constant value of R (e.g., Conrad and Husson, 2009; Steinberger, 2016), or employed radial (e.g., Cammarano et al., 2003) or lateral viscosity variations in the lower mantle (e.g., Moulik and Ekström, 2016;

* Corresponding author at: Centre for Earth Evolution and Dynamics (CEED), University of Oslo, Oslo, Norway.

E-mail address: c.p.conrad@geo.uio.no (C.P. Conrad).

Simmons et al., 2010). In particular, the large low-shear-velocity provinces (LLSVPs) in the lowermost mantle have been attributed to thermal effects, compositionally distinct materials, or a mix of factors (Deschamps et al., 2015; McNamara et al., 2010), all of which imply different distributions of mantle density heterogeneity (Bower et al., 2013; Moulik and Ekström, 2016; Simmons et al., 2010). This diversity of models for the mantle's internal heterogeneity leads to a range of different predictions for the amplitude of the associated dynamic topography (Liu and Zhong, 2016).

Observational constraints on the amplitude and pattern of dynamic topography could potentially help to resolve these uncertainties, and thus place new constraints on mantle processes. However, dynamic topography is difficult to observe directly because it is obscured by larger-amplitude isostatic topography associated with crustal density variations. One approach for detecting the component of topography that is dynamically supported is to use free-air gravity anomalies (Hoggard et al., 2016, 2017), which should be zero for isostatically-supported topography. However, the admittance, which converts free-air gravity anomalies to dynamic topography, is uncertain at long wavelengths, and may range from near zero or even negative values (Colli et al., 2016) to upwards of ~ 100 mgal/km (Molnar et al., 2015). Such values correspond to dynamic topography amplitudes ranging from kilometer scale to negligible for observed gravity anomalies of less than ~ 100 mgal. This suggests the potential for large dynamic topography without large free-air gravity anomalies (Colli et al., 2016), but does not help to constrain the actual amplitude of dynamic topography.

Dynamic topography can be estimated directly if the isostatic component of topographic relief can be confidently estimated and removed. This is significantly simpler for seafloor than it is for continents, where crustal structures have experienced a much longer and more complex development. By contrast, the seafloor topography is dominated by half-space cooling of oceanic lithosphere, which allows us to relate isostatic subsidence of the ridge flank to the square root of seafloor age (e.g., Parsons and Sclater, 1977). Removal of this isostatic topography from seafloor bathymetry produces a map of residual topography (e.g., Flament et al., 2013; Gurnis et al., 2000; Steinberger, 2016) that should directly constrain dynamic topography (e.g., Adam et al., 2015; Hoggard et al., 2016; Steinberger et al., 2017). However, the relationship between subsidence rate and seafloor age may vary between ridge systems (e.g., Calcagno and Cazenave, 1993), and several different relationships have been proposed (e.g., Korenaga and Korenaga, 2008; Parsons and Sclater, 1977; Stein and Stein, 1992; Zhong et al., 2007). Furthermore, rates of seafloor subsidence are determined empirically, and thus incorporate any component of dynamic topography that varies systematically with seafloor age. For these reasons, fully separating isostatic and dynamic topography on the seafloor remains a challenge.

To develop a new constraint on dynamic topography, we utilize the fact that seafloor subsidence should occur at equal rates on both sides of a mid-ocean ridge (MOR), producing isostatic topography that is symmetrical about the ridge axis. Thus, if the seafloor is deflected over long wavelengths by dynamic topography, we would expect to observe an asymmetry in subsidence rates across the MOR (Fig. 1). Indeed, early studies suggested that the western flank of the Mid-Atlantic Ridge (MAR) (Calcagno and Cazenave, 1993; Marty and Cazenave, 1989) and the eastern flank of the East Pacific Rise (EPR) (Cochran, 1986) are subsiding faster than their opposing flanks. Here we examine subsidence trends across large areas of young seafloor in the Pacific and Atlantic basins, and use the resulting observations of subsidence asymmetry to develop a new constraint on the amplitude of dynamic topography that does not depend on a specific choice for the seafloor age-depth relationship.

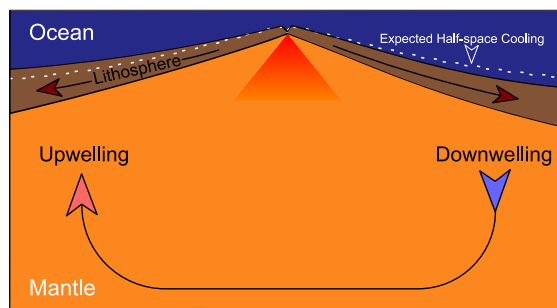


Fig. 1. Cartoon illustrating how dynamic topography creates an apparent asymmetry in half-space cooling across a mid-ocean ridge. The dashed white line represents a symmetric ridge, and the brown ridge shows the seafloor bathymetry after deflection by stresses from mantle flow. In this case, the ridge flank above a downwelling (right) is subsided and the ridge flank above an upwelling (left) is elevated, resulting in a tilted ridge cross section. (For interpretation of the references to color in this figure, the reader is referred to the web version of this article.)

2. Detecting ridge flank asymmetry

To constrain the amplitude of dynamic topography, we utilize the ETOPO1 model of ocean bathymetry sampled at a spacing of a tenth of a degree, or roughly 9–15 km (Sandwell and Smith, 2009). This dataset utilizes constraints from both shiptrack bathymetry and satellite gravity observations. To examine areas relatively unperturbed by local phenomena, we masked bathymetry within 100 km of large igneous provinces (LIPs) and within three times the major axis of seamounts greater than one kilometer in height (Fig. 2b). Varying the masking radii from two to five times the major radius did not significantly impact our results. Because seafloor sediments also impact bathymetry, we excluded areas with more than one kilometer of sediment and isostatically compensated sediments in the remaining areas (Fig. 2b) using the updated NGDC Ocean Sediment map (Whittaker et al., 2013) and the isostatic formulation of Sykes (1996). Abyssal hill processes generate another natural source of variability in depth measurements. We minimized the potential for aliasing by applying a 25 km Gaussian filter and bootstrapping the resulting bathymetry to average out abyssal hills and other geological anomalies along the age profile.

In order to assess the potential bathymetric asymmetry of MORs, we analyzed seafloor spanning the central MAR and EPR (white outlines, Fig. 2), as other regions of the MORs exhibit intense volcanic activity, highly asymmetric age distribution, or complex geometry. For the EPR, we examined seafloor younger than 40 Ma so that profiles would include seafloor on both sides of the ridge. In the Atlantic Basin, we used an age cutoff of 70 Ma to ensure that the dominant physical process would be half-space cooling and not seafloor flattening processes that become important for seafloor older than ~ 80 Ma (Stein and Stein, 1992). We limited the North–South range of the Atlantic Basin to between 30°N and 40°S to minimize the impact of the Icelandic plume.

In order to develop a robust linear regression of bathymetry as a function of the square root of the age of the seafloor, we bootstrapped the bathymetric data by the square root of age by randomly selecting an equal number of data points for each of the 70 and 120 equally spaced square root of age bins for the EPR and MAR, respectively. This mitigates the inherent sampling bias toward younger seafloor (Korenaga and Korenaga, 2008). We performed a simple least-squares linear regression of depth versus the square root of age globally over the age range of 5 to 70 Ma and on each of the four ridge flanks studied. Applying this method globally and using 1000 points in each of the bins, we found a subsidence rate (with one standard deviation uncertainty) for ages < 70 Ma of 319 ± 24 m/Myr $^{1/2}$, which agrees with the rate of 315 ± 26 m/Myr $^{1/2}$ previously reported

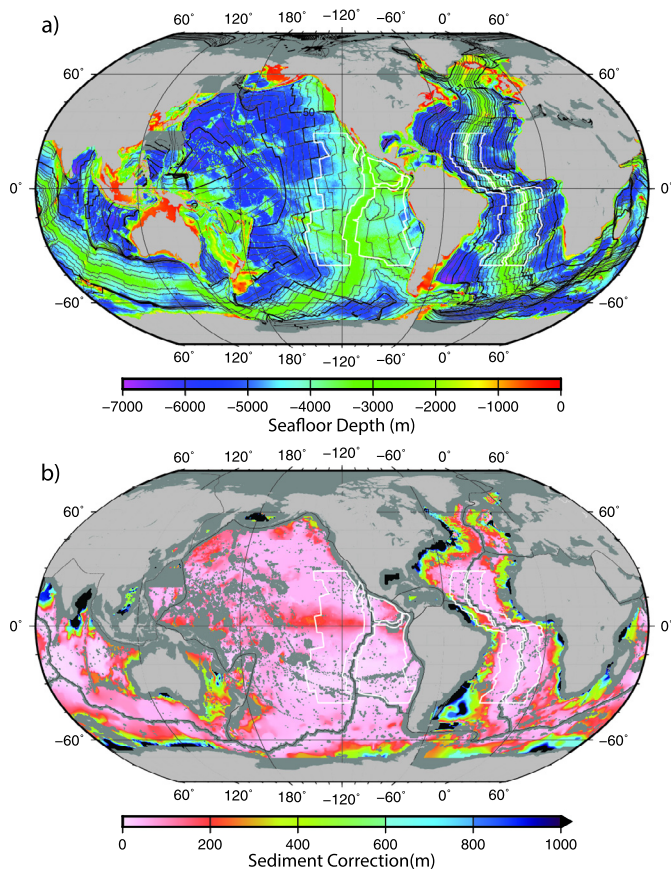


Fig. 2. Maps of seafloor depth, sediment, age, and regions of interest. (a) Seafloor depth from Sandwell and Smith (2009) (colors) and seafloor ages (Müller et al., 2008) (contours with 10 Myr spacing). (b) Sediment depths (Whittaker et al., 2013) are shown in colors, with proscribed regions of LIPs (from the Coffin and Eldholm, 2005 LIP database), seamounts (from the Kim and Wessel, 2011 catalog), and MORs grayed out. The white outlined areas in both (a) and (b) shows the areas of interest for this study, which straddle the East Pacific Rise (EPR) and Mid-Atlantic Ridge (MAR).

by Korenaga and Korenaga (2008). We also tested the results for young seafloor using ETOPO1 against the shiptrack-constrained bathymetry and found negligible differences (Sandwell and Smith, 2009).

As predicted by numerical models of dynamic topography (Fig. 3a) (e.g., Conrad and Husson, 2009; Flament et al., 2013), linear fits to the bathymetry of both the Atlantic (Fig. 4b) and Pacific (Fig. 5b) mid-ocean ridge flanks show a disparity of slope, with the South American side being steeper for both basins. The difference in subsidence rate was more pronounced but also more poorly constrained across the EPR ($50 \pm 10 \text{ m/Myr}^{1/2}$) than across the MAR ($17 \pm 4 \text{ m/Myr}^{1/2}$). The zero-age intercepts of these linear fits additionally indicate a vertical offset between opposing flanks of the two ridges, where the South American side is deeper for the MAR (Fig. 4b) and shallower for the EPR (Fig. 5b).

3. Dynamic topography

We considered dynamic topography as an explanation for the apparent asymmetries across the MAR and EPR by comparing to predictions of dynamic topography from the global mantle flow model of Conrad and Husson (2009). This model is driven by mantle density heterogeneity inferred from the seismic S-wave tomography model S2ORTSb (Ritsema et al., 2004), omits density anomalies above 300 km depth (we consider these later in terms of thermal isostasy), and employs a radial viscosity structure consistent with geoid constraints (e.g., Steinberger, 2016). The

modeled dynamic topography (Fig. 3a) is similar in amplitude and long-wavelength pattern to dynamic topography predicted by other global mantle flow models, as compared recently by Flament et al. (2013). In particular, predicted patterns of dynamic topography (e.g., Fig. 3a) consistently exhibit minima surrounding Southeast Asia and South America, and maxima across the South Pacific super-swell and Africa, mirroring the areas of long-term subduction along the margins of the Pacific Basin and the LLSVPs in the deep mantle, respectively. This basic pattern of dynamic topography predicts asymmetric tilting of both the EPR and MAR ridge systems toward South America.

Because they used a linear rheology, Conrad and Husson (2009) separated mantle flow into four components driven by different sets of density anomalies in the mantle. In particular, they computed dynamic topography supported by mantle flow driven by low-density (Figs. 3b and 3d) and high-density (Figs. 3c and 3e) anomalies, which produce active upwelling and downwelling, respectively, in both the upper (Figs. 3b and 3c) and lower mantle (Figs. 3d and 3e). These four components result in four separate models of mantle flow that predict four different patterns of dynamic topography (termed UMUP, UMDN, LMUP, and LMDN in Fig. 3), which we then normalized so that the maximum amplitude is unity (Figs. 3b–3e). We note that LMUP and LMDN feature rather similar spatial patterns (Figs. 3d and 3e) because long-wavelength upwelling and downwelling flows in the lower mantle tend to complement each other (e.g., Conrad and Husson, 2009).

We use these dynamic topography basis functions (DTBF, Figs. 3b–3e) to constrain the amplitude of dynamic topography necessary to minimize the observed ridge flank asymmetries. To do this, we consider a range of peak dynamic topography amplitudes between -500 m (corresponding to a negative value for the conversion factor R) and 1500 m (corresponding to a large positive R). We subtracted the resulting model predictions of dynamic topography from the regional residual topography and assessed the resulting bathymetric asymmetry across the MAR and EPR. The degree of symmetry between opposing ridge flanks places a constraint on the amplitude of dynamic topography (e.g., Figs. 4 and 5).

To start, we removed the amplitude-scaled LMDN dynamic topography model (Fig. 3e) from the bathymetry and computed linear fits to the age-depth relationship (Fig. 6). As expected (Fig. 4b and 5b), the measured ridge slope for both ridges is steeper on the South American flank without any adjustments for dynamic topography (LMDN amplitude of zero in Figs. 6a and 6b). Removing increasingly larger amplitudes of LMDN dynamic topography tends to rectify this asymmetry by decreasing the slopes on the South American flank of both ridges and increasing the slopes of the opposing ridge flanks. For the MAR, the two slopes match with about $\sim 500 \text{ m}$ of applied dynamic topography (Fig. 6a), and for the EPR we find slope symmetry for $\sim 900 \text{ m}$ total LMDN amplitude (Fig. 6b). Ridge crest depths inferred from linear fits to opposing ridge flanks match for all dynamic topography amplitudes on the MAR (Fig. 6c), but indicate that the western flank of the EPR is on average about 200 m deeper than the eastern flank (Fig. 6d), despite the near-ridge similarity of EPR bathymetry distributions (Fig. 5b).

4. Statistical comparison of bathymetry across a mid-ocean ridge

An analysis of linear fits to bathymetry on opposing sides of a ridge (e.g., Fig. 6) depends on the distribution of bathymetric deviations about these fits, which are of order $\pm 400 \text{ m}$ (Korenaga and Korenaga, 2008). To include these deviations in our analysis, we again compare square root of age linear regressions for opposing ridge flanks after correcting seafloor bathymetry for a given model of dynamic topography (left columns of Figs. 4 and 5). We

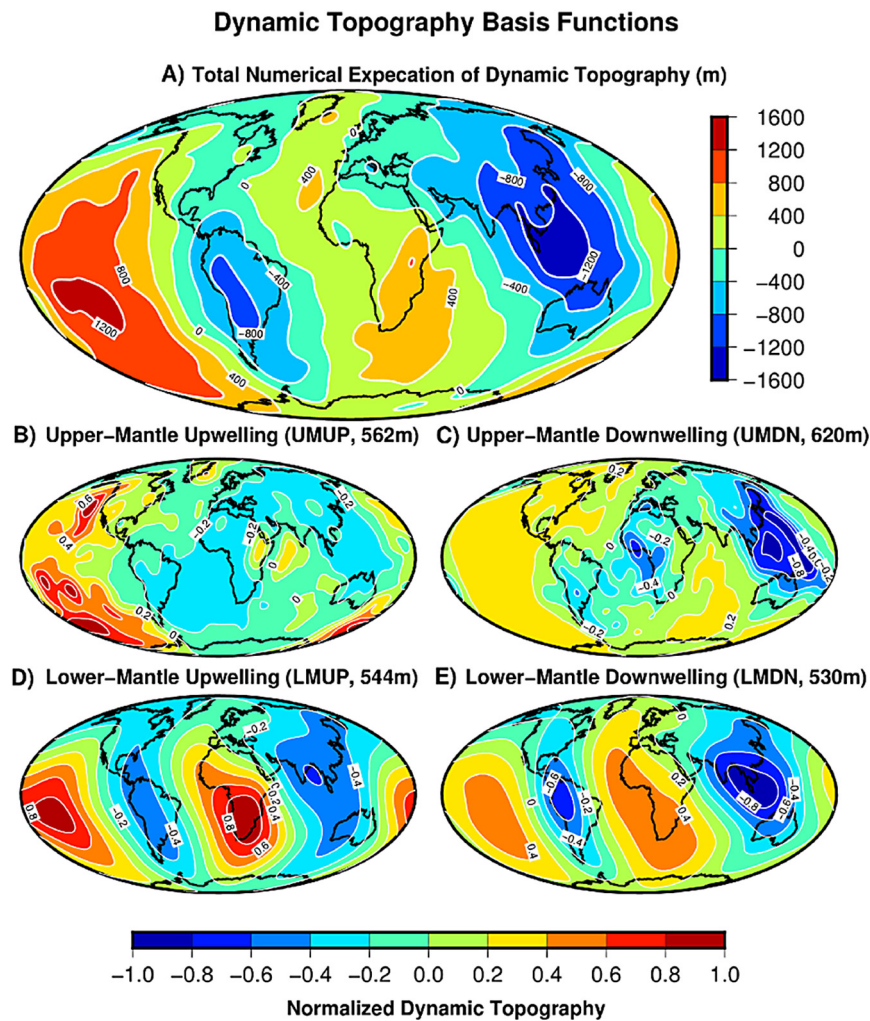


Fig. 3. Dynamic topography predicted by the flow fields from the numerical model of Conrad and Husson (2009), where (A) is the total prediction (whole mantle flow) and (B) through (E) are the dynamic topography basis functions for the components of dynamic topography driven by active upwelling (B and D) or downwelling (C and E) in the upper mantle (B and C) or lower mantle (D and E). These basis functions are normalized by their amplitude (value given) such that the absolute value of maximum dynamic topography is unity.

then compare histograms that show the distribution of bathymetry about the regression developed for the South American flank, which we use as a reference (right columns of Figs. 4 and 5). As the histogram is another representation of the fitting, the distribution for the South American flank has a mean of zero by definition (black line, right columns of Figs. 4 and 5), but the mean for the opposing flank (blue dashed line, right columns of Figs. 4 and 5) is only close to zero if the ridge is bathymetrically symmetrical.

To quantify the degree of symmetry across both ridges, we employ the two-sample Kolmogorov–Smirnov (K–S) test (Oliphant, 2007), which uses the difference in the empirical cumulative distribution functions (CDF), and thus is sensitive to differences in both the position and shape of the two distributions. The maximum difference between the CDF of the two distributions is directly related to the P -value that quantifies the probability that the two distributions are sampled from the same source function. The P -value is also a function of the number of samples in the distribution, and thus of how we bootstrapped the data. However, the appropriate number of independent samples of seafloor is not known but is certainly much smaller than the number of gridded satellite gravity observations (Sandwell and Smith, 2009). Therefore, we treat the number of independent samples per age bin (N_{bin}) as an unknown that varies from 10 to 1000 samples per square-root of age bin (Fig. 7), ranging from undersampling to oversampling the

bathymetry data. This range also relates to the natural length scale of bathymetric variations on the seafloor. For example, transform fault spacing varies with an average of ~ 50 km between ridge offsets (Howell et al., 2016). Along a ridge 8000 km in length (30°N to 40°S), a reasonable range of 25–80 km for the offset length scale gives an expected number of samples from different ridge segments in the range of $N_{\text{bin}} = 100$ to 300 for each bin. This range represents a rough estimate of the minimum number of independent bathymetry measurements necessary to characterize long-wavelength seafloor depth variations in the presence of anomalous short-wavelength topography associated with hot spot swells, transform faulting, and abyssal hills.

To apply the bootstrapping method for a given value of N_{bin} , we randomly sampled N_{bin} bathymetric data points from each square-root of age bin on both flanks, and re-performed the square root of age linear regression. To ensure that the results from a single random sample were not anomalous, we performed the K–S test 1000 times using independently bootstrapped data, and averaged the resulting P -values. We apply this method to both basins after first correcting the bathymetry for a range of amplitudes of dynamic topography for each of the DTBFs (x -axes in Fig. 7). The resulting P -values (y -axes in Fig. 7) express the confidence that the bathymetry distributions on the two opposing flanks (Figs. 4 and 5, right columns) are statistically distinct. Thus a statistically-

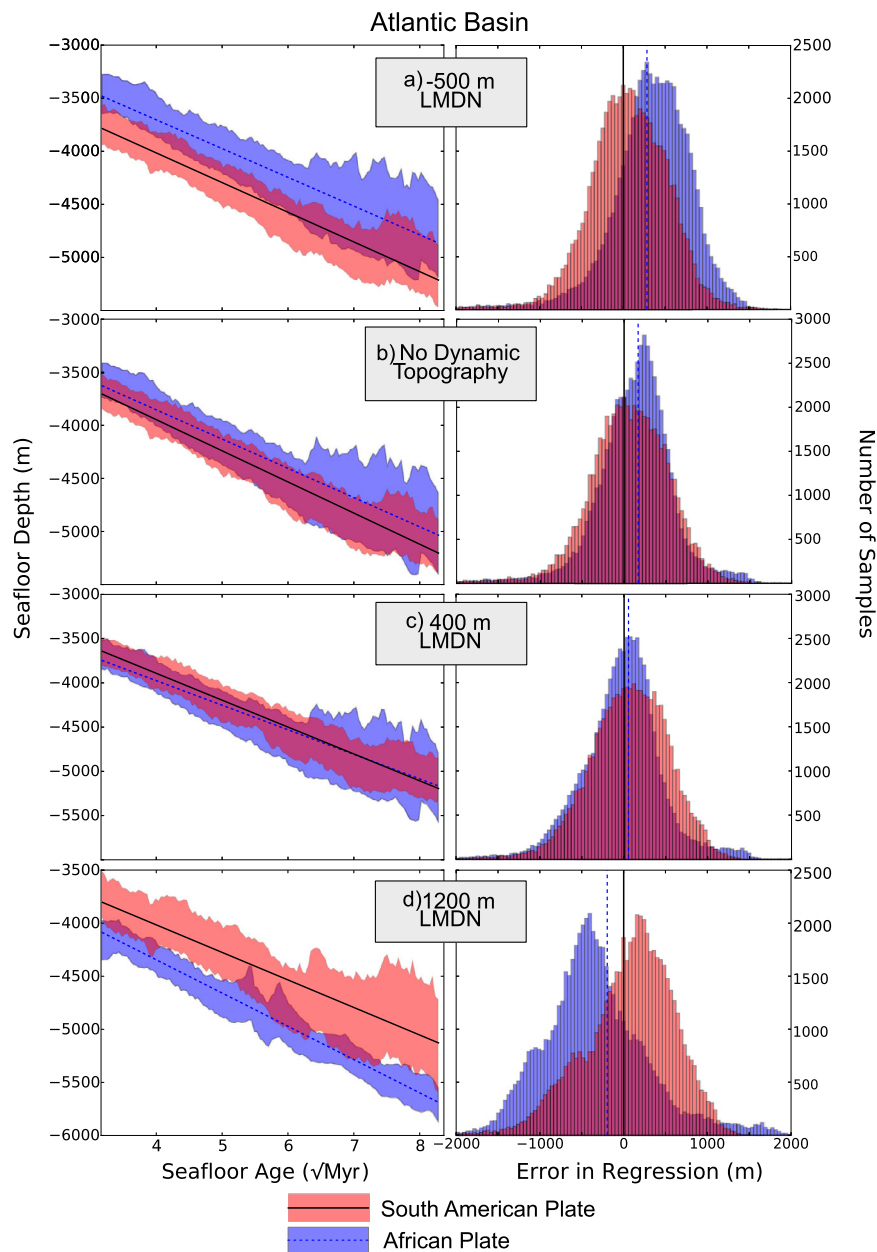


Fig. 4. Comparisons of bathymetric profiles on opposing sides of the Mid-Atlantic Ridge (MAR). On the left panels, the linear regressions for depth versus square-root of age are shown by straight lines (black solid for the South American plate and blue dashed for African plate) and the shaded areas representing the standard deviation of data for the bins (light red and blue for the South American and African flanks, respectively). On the right panels, histograms show the bathymetric difference of each point on both sides of the basin relative to the regression developed for the South American flank. In panel-pairs a) through d) we show the effect of first correcting bathymetry for varying amplitudes of dynamic topography produced by active downwelling in the lower mantle (LMDN, Fig. 3e). We use the distributions represented by these histograms to assess the asymmetry of the ridge basins, using the K-S test (see Fig. 7). (For interpretation of the references to color in this figure, the reader is referred to the web version of this article.)

significant P -value of $P < 0.05$ (Fig. 7) can be considered to produce subsidence patterns on opposite sides of the ridge that are statistically distinguishable from each other with 95% confidence when observed using the associated number of independent samples (N_{bin}). This process provides a rigorous and repeatable statistical tool to find the amplitudes of dynamic topography that must be removed from maps of residual bathymetry to minimize bathymetric differences across the MOR.

We find that runs with fewer samples exhibit systematically higher P -values than runs with more samples (Fig. 7), indicating that the ~ 400 m variance of the bathymetry (Figs. 4 and 5) obscures bathymetric differences across ridges sampled only sparsely (N_{bin} of 10 or 30). On the other hand, distributions sampled more densely (e.g., N_{bin} of 1000) are always distinguishable, and thus

produce low P -values (Fig. 7), because any small difference in the distribution becomes statistically meaningful. Therefore, we find that the most useful information from the K-S test is found with N_{bin} between 100 and 300, which is also the range we estimate as appropriate for the seafloor based on natural length scales.

5. Constraints on the amplitude of dynamic topography

The K-S tests (Fig. 7) indicate the optimal amplitude of dynamic topography needed to minimize ridge asymmetry in either basin assuming spatial patterns of dynamic topography consistent with each of the four DTBFs (Fig. 3). First, we find similar results for upwelling or downwelling pairs in the upper mantle (UMUP and UMDN) and lower mantle (LMUP and LMDN) (Fig. 7). This

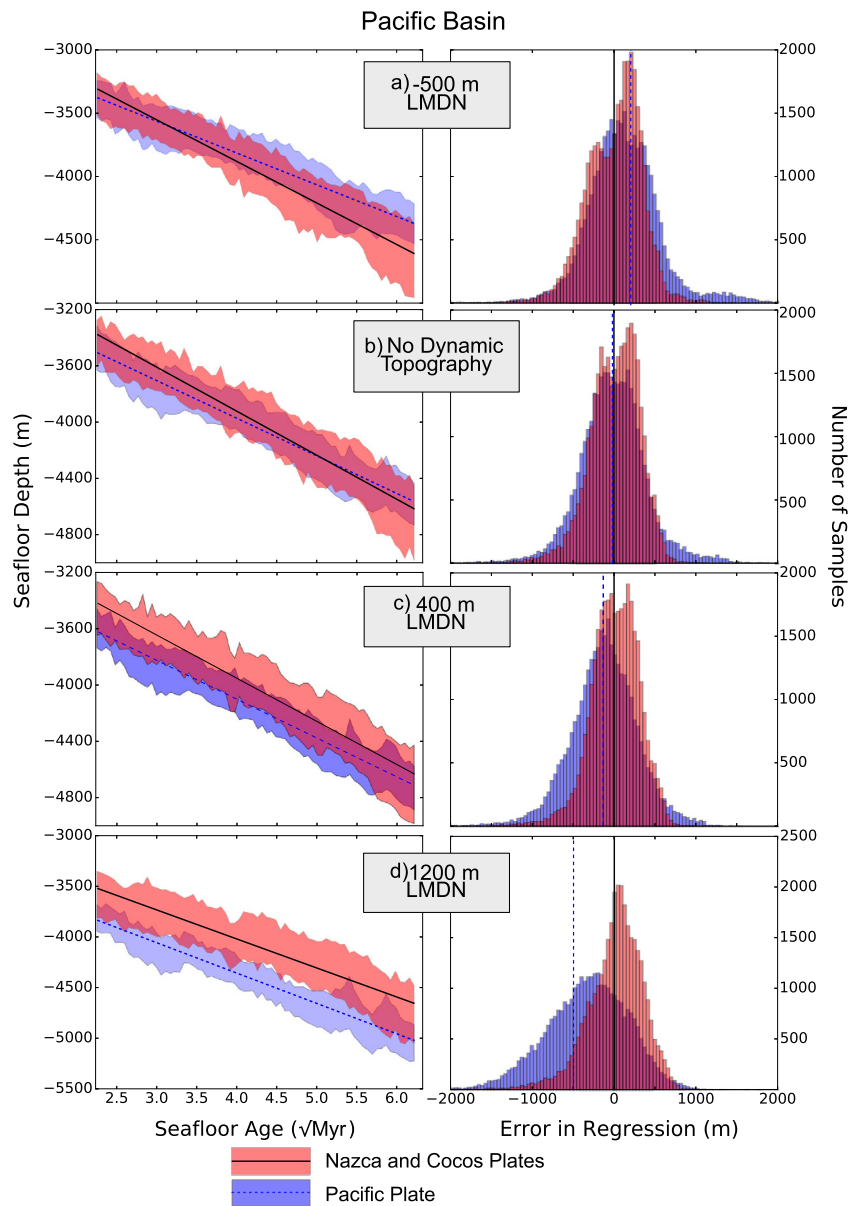


Fig. 5. Comparisons of bathymetric profiles on opposing sides of the East Pacific Rise (EPR). Similar to Fig. 4, but for the Pacific Basin.

indicates that active upwelling typically occurs in the location of return flow from active downwelling (and vice-versa), and both produce similar long-wavelength patterns of dynamic topography (Fig. 3). Thus, constraints from either upwelling or downwelling component provide a useful constraint on the total amplitude of dynamic topography, but we cannot distinguish the relative importance of the two components.

Second, the maxima in P -values (indicating greatest ridge symmetry) indicate different amplitudes of dynamic topography for the Atlantic and Pacific basins, and differ depending on the mantle source of this dynamic topography (Fig. 7). The error distributions across the MAR exhibit a broader range of dynamic topography amplitudes for which the two distributions are statistically indistinguishable, compared to the EPR where P -values exhibit a sharper peak (Fig. 7). This is caused by the MAR's more variable bathymetry, which may be due to the greater abundance of small (<1 km) seamounts on the African plate, as detected by Kim and Wessel (2011). Although these seamounts may contribute to the roughness of the African plate's topographic profile (Fig. 4), they add less than ~10 m to the regionalized elevation of the seafloor

(Conrad et al., 2017) and therefore should not significantly impact our estimates of MAR asymmetry.

For the Atlantic Basin, the amplitude of dynamic topography required to maximize the P -value is about 400–500 m for the lower mantle-sourced DTBFs (Fig. 7, left column), although amplitudes from 0 to 1000 m of lower mantle-induced dynamic topography produce $P > 0.05$ for $N_{\text{bin}} = 300$, and thus represent statistically viable solutions (Fig. 7). Indeed, removal of 400 m of dynamic topography from lower mantle downwelling yields an excellent match for the distributions of both sides of the Atlantic basin (Fig. 4c). The South American side is deeper for smaller dynamic topography (Figs. 4b) or dynamic topography of opposite sign (Fig. 4a), and shallower for larger amplitudes (Fig. 4d). The ~400 m amplitude inferred from the K-S test is consistent with our simple comparison of slopes (Fig. 6a) and ridge crest heights (Fig. 6c) across the MAR.

For the Pacific Basin, the P -value is maximized for dynamic topography amplitudes of only 100–200 m, within a range between –100 and 400 m of statistically viable solutions for $N_{\text{bin}} = 300$ (Fig. 7). These amplitudes are somewhat smaller than the ~900 m

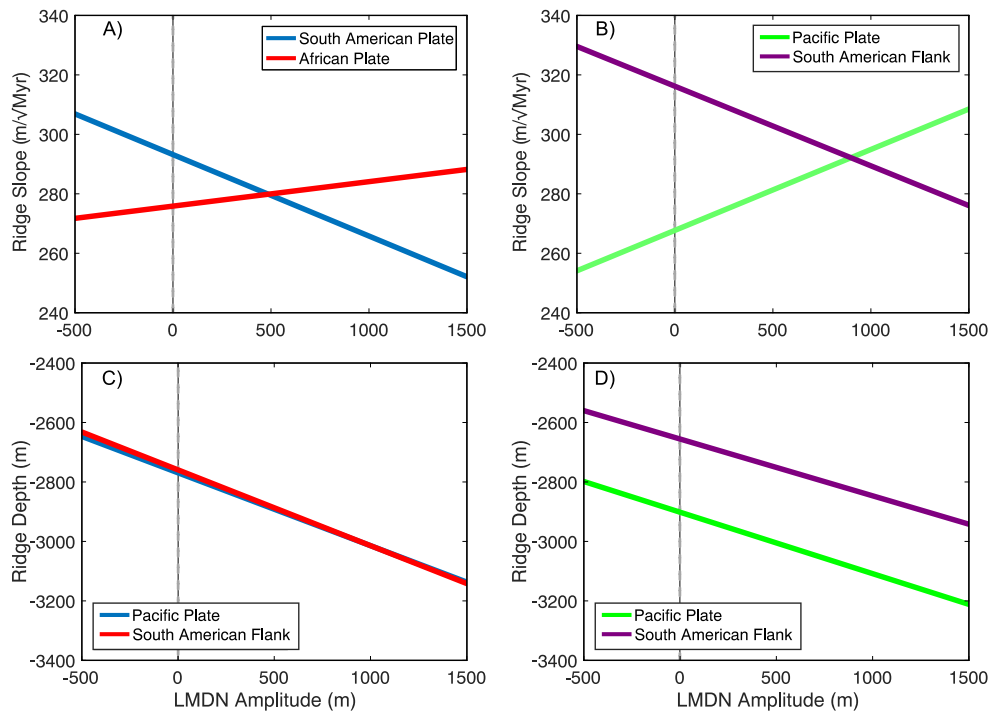


Fig. 6. Ridge subsidence properties, computed as in Figs. 4 and 5 from linear fits to seafloor depth vs. the square root of seafloor age relationships, after correcting bathymetry for dynamic topography of varying amplitude (x -axes). Shown are (A and B) rates of seafloor subsidence and (C and D) depth to the ridge crest (zero-age intercepts of the linear fit) for a range of amplitudes of applied dynamic topography driven by lower mantle downwelling (LMDN) for the (A and C) Mid-Atlantic Ridge and (B and D) East Pacific Rise.

inferred from a simple comparison of ridge slopes (Fig. 6b), but this discrepancy can be attributed to a ~ 200 m downward offset of the Pacific seafloor relative to the Nazca and Cocos seafloor (Fig. 6d). Without accounting for dynamic topography, the fit to the Pacific side is deeper near the ridge crest and shallower away from it compared to the Nazca/Cocos side, leading to much overlap between the distributions of bathymetric deviations (Fig. 5b), and a large P -value from the K-S test (Fig. 7). However, the opposing ridge slopes are closer to parallel after removing 400 m of dynamic topography (Fig. 5c) or more (Fig. 6b), but the K-S test indicates a poorer fit because the overall deeper Pacific side produces an offset of the bathymetry distributions (Fig. 5c).

Although lower mantle flow has the largest influence on long-wavelength dynamic topography (Fig. 3), dynamic topography arising from upper mantle density heterogeneity can contribute to ridge asymmetry on shorter wavelengths. We find that upper mantle flow affects asymmetry of the MAR and EPR differently, with maximum P -values at about -300 and $+100$ m of dynamic topography, respectively (Fig. 7). The negative dynamic topography constrained in the Atlantic results from the upper mantle DTBFs (Figs. 3b and 3c), which predict an extension of the Congo basin subsidence into the eastern Atlantic basin and a pattern of dynamic topography opposite to that of the lower mantle (Figs. 3e). Upper mantle dynamic topography therefore must be applied with negative amplitude to correct the deeper bathymetry on the western side of the MAR (Fig. 7). Introducing contributions from both upper mantle components (UMUP and UMDN) to the LMDN calculation slightly increases the best-fitting amplitude of dynamic topography from lower mantle sources from ~ 400 m to ~ 500 m for the MAR, which is still within the range given by the K-S test. By contrast, the inferred amplitude of LMDN dynamic topography inferred from the EPR decreases slightly due to the inclusion of upper mantle sources, because contributions from upper and lower sources have the same pattern and sign in the Pacific (Fig. 3). Thus, flow from upper mantle density heterogeneity (300–670 km depth)

does not significantly alter our estimates of the total dynamic topography necessary to explain ridge flank asymmetry.

6. Discussion

Our analysis suggests that both the MAR and EPR are tilted asymmetrically toward South America. This pattern is broadly consistent with numerical models of mantle flow that predict negative dynamic topography across that continent, supported by subduction-driven downwelling in the underlying mantle (Fig. 3a). The amplitudes of the observed ridge asymmetries, however, indicate amplitudes of long-wavelength dynamic topography (~ 500 m for the MAR) that are significantly smaller than those indicated by numerical models (~ 1200 m and larger). Indeed, removing ~ 1200 m of inferred dynamic topography over-corrects the measured ridge asymmetry significantly (Figs. 4d and 5d). Thus, unless some other process is obscuring the surface expression of long-wavelength dynamic topography, amplitudes of long-wavelength dynamic topography should be less than half of values estimated from mantle flow models. Below we consider both of these possibilities.

6.1. Crustal thickness asymmetry

It is possible that asymmetries in crustal thickness or asthenospheric dynamics support isostatic topographic asymmetry that masks underlying dynamic topography with greater amplitudes than we observe here (Guerrero et al., 2016). For example, our results would be consistent with larger long-wavelength dynamic topography if the oceanic crust were thicker on the South American side of both the MAR and EPR, obscuring some of bathymetric asymmetry across those ridges. Indeed, accounting for 200 to 400 m of extra elevation on the western flank of the MAR (Fig. 4d) and the eastern flank of the EPR (Fig. 5d) would make our results approximately consistent with ~ 1200 m amplitudes of long-wavelength dynamic

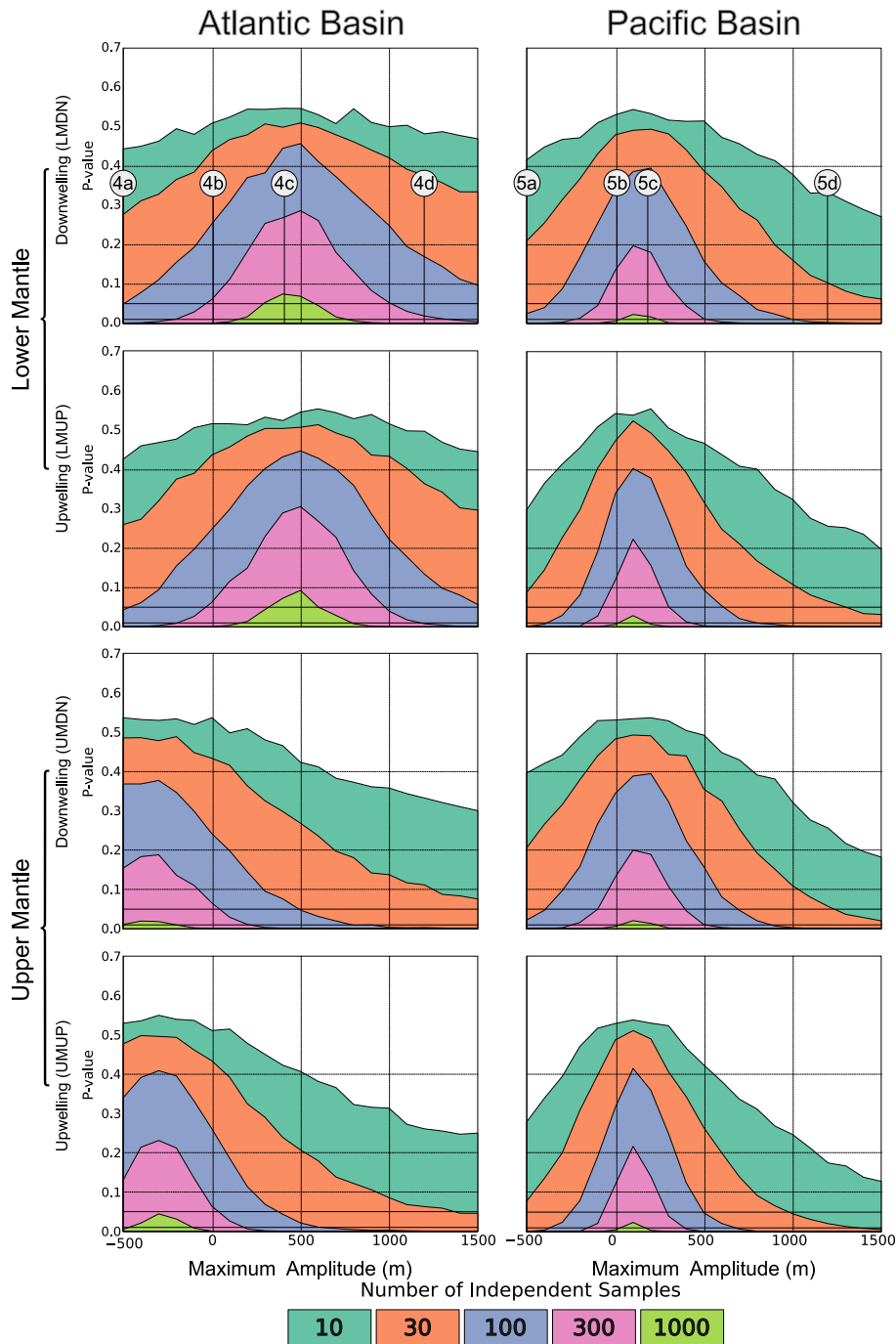


Fig. 7. Application of the two-sample Kolmogorov–Smirnov (K–S) test (Oliphant, 2007), which we use to quantify the statistical difference between bathymetric distributions of opposing MOR flanks, as a function of the maximum amplitude of dynamic topography removed from the bathymetry (x -axis). We compute the K–S test for the MAR (left column) and the EPR (right column), for each of the four dynamic topography basis functions of Fig. 3 (rows). Circles in the top row correspond to figure panels (from Figs. 4 and 5) that show the cross-ridge bathymetric comparison for the given amplitude of LMDN dynamic topography. We compute the P -value of the K–S test for several different values of the number of independent samples (N_{bin} between 10 to 1000 samples per bin) because the appropriate value for N_{bin} is unknown. A larger P -value indicates greater statistical similarity between the distributions. Pairs of cross-basin distributions with P -values that fall below the horizontal black line at $P = 0.05$ can be distinguished with 95% confidence, indicating an asymmetrical ridge. Those above this level are similar enough that sampling from a symmetrical ridge cannot be excluded.

topography. Although these values represent a cross-ridge asymmetry in total crustal thickness of less than 10%, there is currently no strong evidence for such asymmetry occurring across the MAR or EPR. Canales et al.'s (1998) seismic survey of the MELT study area, a ~ 500 km region that traverses the EPR, detected slightly thicker crust on the Nazca side of the EPR but could not confidently resolve an asymmetry across the ridge within their error bounds of several hundred meters. However, the small asymmetry that Canales et al. (1998) did detect (a few hundred meters) is

approximately consistent with the ridge crest offset that we measured across the EPR (Fig. 6d), and accounting for this offset should produce an excellent bathymetric match to the two sides of that ridge for dynamic topography with amplitude of ~ 400 m (Figs. 5c) or more (Fig. 5d). Of course, we do not know if the crustal thicknesses observed in the MELT study area are representative of the entire EPR, nor there are any good constraints on crustal thickness asymmetry for the MAR. Indeed, a physical mechanism for maintaining a crustal thickness asymmetry has only been proposed for

individual ridge segments (Carbotte et al., 2004), not for an entire ridge system like the EPR or MAR.

6.2. Thermal asymmetry of the asthenosphere or lower lithosphere

It is also possible that thermal heterogeneity in the asthenosphere can produce long-wavelength deflections of the seafloor (Molnar et al., 2015). This could occur if the lower lithosphere or upper asthenosphere is thermally asymmetric across the MAR and EPR, causing one side to be isostatically elevated. For example, hot mantle beneath the Nazca plate could elevate the South American side of the EPR, obscuring long-wavelength gradients of dynamic topography supported by deeper mantle flow (Fig. 3). We can estimate an upper bound for the amplitude of these surface deflections by assuming isostatic compensation for thermal heterogeneity in the asthenosphere. Asthenospheric flow should decrease their amplitudes for deeper and shorter wavelength anomalies, but surface deflections should remain larger than ~40–60% of the isostatic limit for basin-scale thermal heterogeneity shallower than 300 km depth (Steinberger, 2016). Assuming a uniform layer of thickness H_{layer} and excess temperature ΔT between two flanks of a ridge, an isostatic balance elevates the hotter side by up to $\Delta h = \alpha * H_{\text{layer}} * \Delta T * \frac{\rho_{\text{asth}}}{(\rho_{\text{asth}} - \rho_{\text{water}})}$, where $\alpha = 3 \times 10^{-5} \text{ K}^{-1}$ is the thermal expansion coefficient, and $\rho_{\text{asth}} = 3300$ and $\rho_{\text{water}} = 1000 \text{ kg/m}^3$ are the densities of asthenosphere and water, respectively. A 100 km thick layer beneath the Nazca plate with excess temperature of ~50°C would elevate the EPR's eastern flank by up to ~200 m, enough to explain the ridge crest asymmetry across the EPR (Fig. 4d). However, a temperature asymmetry of ~50°C translates to a density asymmetry of ~0.15%, which would be observable as a seismic velocity heterogeneity of ~0.75% assuming $R = 0.2$. Although surface wave tomography models may not be sensitive enough to detect systematic asymmetry of only 0.75% across a ridge, no such asymmetry across the EPR is apparent in Schaeffer and Lebedev's (2013) models, and may even be oppositely oriented if present.

Asymmetry of the EPR has been attributed to asymmetric transport of hot mantle toward the EPR from the west, and is supported by seismic observations (e.g., Scheirer et al., 1998) and models (e.g., Conder et al., 2002). Indeed, early observations of asymmetric subsidence across the EPR were attributed to hotter mantle underlying that ridge's western flank (Cochran, 1986). Such a temperature gradient across the ridge could account for some of the slope difference across the ridge and may help to reconcile the larger dynamic topography implied by the EPR (~900 m, Fig. 6b) compared to the more symmetric MAR (~500 m, Fig. 6a). Furthermore, the viscosity asymmetry associated with this cross-ridge temperature gradient should cause extensional plate-driving forces to be more strongly coupled to the colder asthenosphere east of the EPR, which would elevate the eastern flank (Eberle and Forsyth, 1998) and may help explain the observed ridge offset (Fig. 6d).

6.3. Reduced density heterogeneity in the mantle

After accounting for possible crustal thickness or deeper thermal asymmetries across the MAR and EPR, we constrain amplitudes of long-wavelength dynamic topography (~500 m) that are smaller than those predicted from numerical simulations (~1200 m or more). Adjusting either the mantle's radial viscosity structure or its density structure may reduce the amplitude of dynamic topography predicted by such models. Changes to the viscosity structure strongly affect the geoid, which is better constrained than dynamic topography (e.g., Steinberger, 2016). Dynamic topography, however, scales directly mantle density heterogeneity (Hager et al., 1985), and therefore we explore the possibility that the amplitude of density heterogeneity used by global

models such as Conrad and Husson (2009) may be too large. As discussed earlier, Conrad and Husson's (2009) mantle flow models assume a constant value of R for all regions, mineral compositions, and mineral phases in the mantle. Our constraints on the amplitude of dynamic topography suggest that either a smaller value of R should be used across the mantle, or that its effective value should be reduced in some portions of the mantle, such as the LLSVP regions of the lower mantle. Indeed, several authors have noted that a negligible to negative seismic conversion factor, $R \leq 0$, may apply for some of the low-velocity anomalies in the lower mantle (Moulik and Ekström, 2016). This would cause the LLSVPs, and possibly also the seismically-slow regions above them, to act as chemically distinct and stable thermochemical piles (Deschamps et al., 2015) that would contribute little to long-wavelength dynamic topography.

Active downwelling and active upwelling driven by density heterogeneity within the lower mantle (LMUP and LMDN), as computed by Conrad and Husson (2009), produce similar patterns of dynamic topography (Figs. 3d and 3e) with similar ~500 m amplitudes. Our finding that the seafloor is only deflected on long wavelengths at amplitudes of ~500 m suggests a contribution from only one of these dynamic topography components. Given that the LLSVP regions have been proposed to be neutrally buoyant (Moulik and Ekström, 2016), and therefore may produce little or no active upwelling, we suggest that the observed asymmetry across the mid-ocean ridges is perhaps best explained by active downwelling in the lower mantle. Such a model of lower mantle dynamics produces a pattern of long-wavelength dynamic topography (Fig. 3e) similar to the pattern inferred from models with both active upwelling and downwelling (Fig. 3a), but with significantly reduced amplitudes. Indeed, the downwelling-dominated model produces dynamic highs and lows with amplitudes that are consistent with amplitudes inferred from our analysis of basin asymmetry. It is interesting to note that a downwelling-dominated model is consistent with early global flow models based on subduction history, which were adopted before tomographic constraints on mantle density heterogeneity were available (e.g., Ricard et al., 1993).

Without active upwelling flow in the lower mantle, the amplitude of long-wavelength dynamic topography predicted by global mantle flow models becomes significantly reduced. To determine whether this reduction explains the observed asymmetry of the ocean basins, we re-computed dynamic topography by summing three basis functions (LMDN, UMUP, and UMDN but excluding LMUP) using Conrad and Husson (2009) assumption that a constant seismic conversion factor (R) applies for all depths. Using the Atlantic basin asymmetry as a constraint (and thus avoiding the ridge crest offset that complicates the EPR), we calculated the P -value that compares the bathymetry distributions between the two sides of the Atlantic basin, as before, for a range of conversion factors applied uniformly to all three basis functions. We find (Fig. 8) ridge symmetry (as indicated by $P > 0.05$) for values of R_{dim} ranging from 0.05 to 0.13 $\text{g cm}^{-3} \text{ km}^{-1} \text{ s}$, which is below the value of $R_{\text{dim}} = 0.15 \text{ g cm}^{-3} \text{ km}^{-1} \text{ s}$ used by Conrad and Husson (2009). Note that R_{dim} is related to the dimensionless R by a factor of the reference density divided by shear velocity (ρ/v_s), which has a relatively constant value of ~0.75 $\text{g cm}^{-3} \text{ km}^{-1} \text{ s}$ through the mantle. Thus, $R_{\text{dim}} = 0.15 \text{ g cm}^{-3} \text{ km}^{-1} \text{ s}$ used by Conrad and Husson (2009) corresponds to $R = 0.2$, consistent with recent studies (e.g., Steinberger, 2016). Our analysis of MAR ridge asymmetry (Fig. 8) suggests a smaller value of R between 0.07 and 0.17, which is consistent with some studies (e.g., Perry et al., 2003) and within the (low end of the) range of uncertainty of mineral physics constraints (e.g., Karato and Karki, 2001).

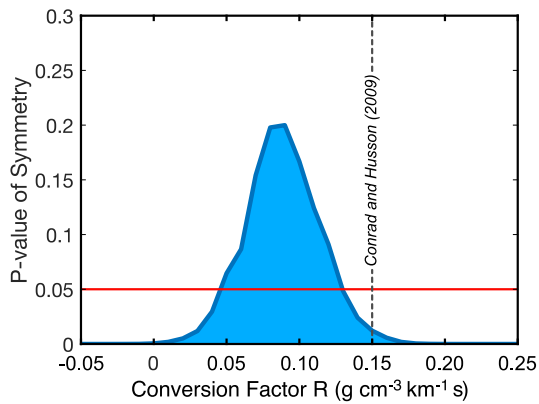


Fig. 8. Bathymetric asymmetry of the Atlantic Basin as a function of the seismic conversion factor used to convert tomographic anomalies into density heterogeneity that drives mantle flow. Here the density heterogeneity model includes both active upwelling and downwelling in the upper mantle (UMUP and UMDN) and active downwelling in the lower mantle (LMDN), but excludes active upwelling in the lower mantle (LMUP). Shown is the P -value measured using the K-S test assuming $N_{\text{bin}} = 300$, and computed as for Fig. 7.

6.4. Implications for the subsidence rate of oceanic lithosphere

Our method for estimating the amplitude of long-wavelength dynamic topography from bathymetry observations avoids two complications inherent to previous constraints based on residual topography (e.g., Flament et al., 2013). First, our model does not depend on models for isostatic topography in continental regions, which are poorly constrained but also contribute significantly to spherical harmonic representations of residual topography (e.g., Hoggard et al., 2016; Steinberger, 2016; Steinberger et al., 2017). Second, our method does not require us to remove one of several different age-depth relationships (e.g., Parsons and Sclater, 1977; Stein and Stein, 1992; Zhong et al., 2007) from the observed bathymetry. This is important because age-depth relationships are empirically determined and therefore removing them may eliminate systematic variations of long-wavelength dynamic topography with seafloor age.

Instead, we compute age-depth relationships for bathymetrically-symmetric ridges after long-wavelength dynamic topography has been removed, which should provide a more direct constraint on the thermal cooling process responsible for subsidence. Such constraints are evident from the comparison of ridge slopes and crest depths from opposing sides of the MAR and EPR, as a function of dynamic topography amplitude (Fig. 6). The MAR presents a consistent picture of both ridge flanks subsiding symmetrically away from a ridge crest approximately ~ 2900 m deep (Fig. 6c) at a rate of ~ 280 m/Myr $^{1/2}$ (Fig. 6a), after ~ 500 m of long-wavelength dynamic topography has been removed. It is more difficult to discern a symmetrical relation that applies for both sides of the EPR (for the reasons discussed above), but we note that the MAR relation approximately describes the Pacific flank of the EPR for dynamic topography amplitude of 500 m (Fig. 6b and 6d).

Our estimate of a subsidence rate of ~ 280 m/Myr $^{1/2}$ for the MAR (Fig. 6a) is markedly lower than most previous estimates of the global subsidence rate, which are in the range of ~ 320 m/Myr $^{1/2}$ (e.g., Korenaga and Korenaga, 2008). This smaller subsidence rate occurs for two reasons. First, previous studies have estimated subsidence rates based on global data, whereas our estimate is based on only two ridge systems (MAR and EPR) that are not well-represented among the most steeply dipping ridge segments globally (Marty and Cazenave, 1989). Second, the MAR is closer to the African dynamic high than it is to the South American low (Fig. 3e), which means that removal of long-wavelength dynamic topography tends to cause the subsidence rate for the

South American flank of the MAR to decrease more than the rate for the African flank is increased. In effect, dynamic topography accounts for part of the observed seafloor subsidence away from the MAR, and accounting for this tends to decrease the total subsidence rate attributed to thermal contraction (Fig. 6a). This effect is smaller for the EPR, although that ridge is complicated by asymmetry in zero-age offset, as discussed above. A slow subsidence rate can be associated with decreased effective values for thermal expansivity or the thermal diffusivity (e.g., Grose, 2012).

7. Conclusions

By comparing bathymetric subsidence curves on opposing ridge flanks of the Mid-Atlantic Ridge (MAR) and East Pacific Rise (EPR), we show that the South American flank of both ridges is steeper than the opposing flank. This ridge asymmetry can be explained by long-wavelength dynamic topography driven by convection patterns arising from density heterogeneity in the lower mantle. By correcting bathymetry for patterns of dynamic topography predicted using the numerical mantle flow model of Conrad and Husson (2009), we found that long-wavelength dynamic topography with peak amplitudes of about 500 m can explain the bathymetric asymmetry across the MAR (Fig. 7). Removal of this dynamic topography results in ridges that subside approximately symmetrically at ~ 280 m/Myr $^{1/2}$ from a ridge crest 2900 m below sea level (Fig. 6).

The observed bathymetric asymmetry of the EPR is not as easily related to long-wavelength dynamic topography. Indeed, the subsidence rates of the two sides of the ridge match most closely after removing long-wavelength dynamic topography with ~ 900 m peak amplitude (Fig. 6b), and yet the statistical similarity between the distributions of residual bathymetry across the ridge is maximized for only 100–200 m of dynamic topography (Fig. 7). This discrepancy largely results from elevated bathymetry on the Nazca/Cocos side of the EPR, which yields a steeper but shallower eastern flank. Attributing this elevated bathymetry to a ~ 200 m offset across the ridge, possibly resulting from systematically thicker crust (Cochran, 1986) or deeper coupling of tectonic stresses on the eastern flank (Eberle and Forsyth, 1998), yields an eastward-tilting EPR that can be made symmetric by accounting for 900 m of dynamic topography. Some of this tilting, however, may be due to isostatic support of shallow cross-ridge temperature gradients (Cochran, 1986) associated with eastward transport of upwelling heat from the central Pacific (Conder et al., 2002; Scheirer et al., 1998). If so, then the EPR and MAR may exhibit approximately similar subsidence relationships, and a degree of asymmetry that implies long-wavelength dynamic topography with an amplitude of ~ 500 m.

The ~ 500 m amplitude of long-wavelength dynamic topography that we infer from observations of asymmetrical subsidence of the EPR and MAR is consistent with amplitudes inferred from recent global studies of residual seafloor topography of the seafloor (e.g., Guerri et al., 2016; Hoggard et al., 2016; Steinberger, 2016; Steinberger et al., 2017). It is also consistent with Yang et al.'s (2017) reconstruction of only minor negative residual topography at long wavelengths for the bathymetry around South America, despite larger amplitudes elsewhere. However, ~ 500 m of dynamic topography is less than half of that suggested by most numerical models of global mantle convection (e.g., Flament et al., 2013), and resolving this discrepancy remains a challenge. Because the amplitude of dynamic topography scales with the magnitude of density heterogeneity in the mantle, mantle models with diminished density heterogeneity may help to explain decreased amplitudes of dynamic topography. We find that slab-driven and downwelling-dominated lower mantle flow yields long-wavelength dynamic topography with the correct amplitude and spatial pat-

tern. This conception of mantle flow is consistent with global flow models based on subduction history (e.g., Ricard et al., 1993), as well as thermochemical convection models without broad active upwelling at long-wavelengths (e.g., McNamara et al., 2010). However, such models may not be consistent with constraints from the geoid (Guerra et al., 2016; Liu and Zhong, 2016), and most thermochemical representations of mantle convection maintain chemically differentiated material only in the LLSVP regions of the lowermost mantle (e.g., Deschamps et al., 2015). Therefore, it may be necessary to consider alternative models for thermochemical convection that employ, for example, strong lateral viscosity variations (e.g., Ballmer et al., 2017). Patterns of anomalous long-wavelength bathymetry from across the global seafloor should place important constraints on thermochemical convection models in the future.

Acknowledgements

The authors thank R. Moucha and one anonymous referee for constructive reviews, and P. Wessel, N. Frazer, and B. Steinberger for comments that improved the manuscript. This work was partly supported by NSF Grant EAR-1151241 and the Research Council of Norway through its Centres of Excellence funding scheme, project number 223272.

References

- Adam, C., King, S.D., Vidal, V., Rabinowicz, M., Jalobeanu, A., Yoshida, M., 2015. Variation of the subsidence parameters, effective thermal conductivity, and mantle dynamics. *Earth Planet. Sci. Lett.* 426, 130–142. <https://doi.org/10.1016/j.epsl.2015.06.025>.
- Ballmer, M.D., Houser, C., Hernlund, J.W., Wentzcovitch, R.M., Hirose, K., 2017. Persistence of strong silica-enriched domains in the Earth's lower mantle. *Nat. Geosci.* 10 (3), 236–240. <https://doi.org/10.1038/ngeo2898>.
- Bower, D.J., Gurnis, M., Seton, M., 2013. Lower mantle structure from paleogeographically constrained dynamic Earth models. *Geochem. Geophys. Geosyst.* 14 (1), 44–63. <https://doi.org/10.1029/2012GC004267>.
- Calcagno, P., Cazenave, A., 1993. Present and past regional ridge segmentation: evidence in Geoid data. *Geophys. Res. Lett.* 20 (18), 1895–1898. <https://doi.org/10.1029/93GL00988>.
- Cammarano, F., Goes, S., Vacher, P., Giardini, D., 2003. Inferring upper-mantle temperatures from seismic velocities. *Phys. Earth Planet. Inter.* 138 (3), 197–222. [https://doi.org/10.1016/S0031-9201\(03\)00156-0](https://doi.org/10.1016/S0031-9201(03)00156-0).
- Canales, J.P., Detrick, R.S., Bazin, S., Harding, A.J., Orcutt, J.A., 1998. Off-axis crustal thickness across and along the East Pacific rise within the MELT area. *Science* 280 (5367), 1218–1221. <https://doi.org/10.1126/science.280.5367.1218>.
- Carbotte, S.M., Small, C., Donnelly, K., 2004. The influence of ridge migration on the magmatic segmentation of mid-ocean ridges. *Nature* 429 (6993), 743–746. <https://doi.org/10.1038/nature02652>.
- Cochran, J.R., 1986. Variations in subsidence rates along intermediate and fast spreading mid-ocean ridges. *Geophys. J. R. Astron. Soc.* 87 (2), 421–454. <https://doi.org/10.1111/j.1365-246X.1986.tb06631.x>.
- Coffin, M.F., Eldholm, O., 2005. Large igneous provinces. In: Seiley, R.C., Cocks, R., Plimer, I.R. (Eds.), *Encyclopedia of Geology*. Elsevier, Oxford, pp. 315–325.
- Colli, L., Ghelichkhan, S., Bunge, H.P., 2016. On the ratio of dynamic topography and gravity anomalies in a dynamic Earth. *Geophys. Res. Lett.*, 2016GL067929. <https://doi.org/10.1002/2016GL067929>.
- Conder, J.A., Forsyth, D.W., Parmentier, E.M., 2002. Asthenospheric flow and asymmetry of the East Pacific Rise, MELT area. *J. Geophys. Res., Solid Earth* 107 (B12). <https://doi.org/10.1029/2001JB000807>. 8–1-ETG 8–13.
- Conrad, C.P., Husson, L., 2009. Influence of dynamic topography on sea level and its rate of change. *Lithosphere* 1, 110–120. <https://doi.org/10.1130/L32.1>.
- Conrad, C.P., Selway, K., Hirschmann, M.M., Ballmer, M.D., Wessel, P., 2017. Constraints on volumes and patterns of asthenospheric melt from the space-time distribution of seamounts. *Geophys. Res. Lett.* 44 (14), 7203–7210. <https://doi.org/10.1002/2017GL074098>.
- Deschamps, F., Li, Y., Tackley, P., 2015. Large-scale thermo-chemical structure of the deep mantle: observations and models. In: *The Earth's Heterogeneous Mantle*. Springer, pp. 479–515.
- Eberle, M.A., Forsyth, D.W., 1998. Evidence from the asymmetry of fast-spreading ridges that the axial topographic high is due to extensional stresses. *Nature* 394, 360. <https://doi.org/10.1038/28596>.
- Flament, N., Gurnis, M., Mueller, R.D., 2013. A review of observations and models of dynamic topography. *Lithosphere* 5 (2), 189–210. <https://doi.org/10.1130/L245.1>.
- Grose, C.J., 2012. Properties of oceanic lithosphere: revised plate cooling model predictions. *Earth Planet. Sci. Lett.* 333–334, 250–264. <https://doi.org/10.1016/j.epsl.2012.03.037>.
- Guerra, M., Cammarano, F., Tackley, P.J., 2016. Modelling Earth's surface topography: decomposition of the static and dynamic components. *Phys. Earth Planet. Inter.* 261 (Part B), 172–186. <https://doi.org/10.1016/j.pepi.2016.10.009>.
- Gurnis, M., Mitrovica, J.X., Ritsema, J., van Heijst, H.-J., 2000. Constraining mantle density structure using geological evidence of surface uplift rates: the case of the African Superplume. *Geochem. Geophys. Geosyst.* 1 (7), 1020. <https://doi.org/10.1029/1999GC000035>.
- Hager, B.H., Clayton, R.W., Richards, M.A., Comer, R.P., Dziewonski, A.M., 1985. Lower mantle heterogeneity, dynamic topography and the geoid. *Nature* 313 (6003), 541–545. <https://doi.org/10.1038/313541a0>.
- Hoggard, M.J., White, N., Al-Attar, D., 2016. Global dynamic topography observations reveal limited influence of large-scale mantle flow. *Nat. Geosci.* 9 (6), 456–463. <https://doi.org/10.1038/ngeo2709>.
- Hoggard, M.J., Winterbourne, J., Czarnota, K., White, N., 2017. Oceanic residual depth measurements, the plate cooling model, and global dynamic topography. *J. Geophys. Res., Solid Earth* 122 (3), 2328–2372. <https://doi.org/10.1002/2016JB013457>.
- Howell, S.M., Ito, G., Behn, M.D., Martinez, F., Olive, J.-A., Escartín, J., 2016. Magmatic and tectonic extension at the Chile Ridge: evidence for mantle controls on ridge segmentation. *Geochem. Geophys. Geosyst.* 17 (6), 2354–2373. <https://doi.org/10.1002/2016GC006380>.
- Karato, S.-i., Karki, B.B., 2001. Origin of lateral variation of seismic wave velocities and density in the deep mantle. *J. Geophys. Res., Solid Earth* 106 (B10), 21771–21783. <https://doi.org/10.1029/2001JB000214>.
- Kim, S.-S., Wessel, P., 2011. New global seamount census from altimetry-derived gravity data. *Geophys. J. Int.* 186 (2), 615–631. <https://doi.org/10.1111/j.1365-246X.2011.05076.x>.
- Korenaga, T., Korenaga, J., 2008. Subsidence of normal oceanic lithosphere, apparent thermal expansivity, and seafloor flattening. *Earth Planet. Sci. Lett.* 268 (1–2), 41–51. <https://doi.org/10.1016/j.epsl.2007.12.022>.
- Liu, L., 2015. The ups and downs of North America: evaluating the role of mantle dynamic topography since the Mesozoic. *Rev. Geophys.* 53 (3), 2015RG000489. <https://doi.org/10.1002/2015RG000489>.
- Liu, X., Zhong, S., 2016. Constraining mantle viscosity structure for a thermochemical mantle using the geoid observation. *Geochem. Geophys. Geosyst.* 17 (3), 895–913. <https://doi.org/10.1002/2015GC006161>.
- Marty, J.C., Cazenave, A., 1989. Regional variations in subsidence rate of oceanic plates: a global analysis. *Earth Planet. Sci. Lett.* 94 (3), 301–315. [https://doi.org/10.1016/0012-821X\(89\)90148-9](https://doi.org/10.1016/0012-821X(89)90148-9).
- McNamara, A.K., Garnero, E.J., Rost, S., 2010. Tracking deep mantle reservoirs with ultra-low velocity zones. *Earth Planet. Sci. Lett.* 299 (1–2), 1–9. <https://doi.org/10.1016/j.epsl.2010.07.042>.
- Molnar, P., England, P.C., Jones, C.H., 2015. Mantle dynamics, isostasy, and the support of high terrain. *J. Geophys. Res., Solid Earth* 120 (3), 1932–1957. <https://doi.org/10.1002/2014JB011724>.
- Moulik, P., Ekström, G., 2016. The relationships between large-scale variations in shear velocity, density, and compressional velocity in the Earth's mantle. *J. Geophys. Res., Solid Earth* 121 (4), 2737–2771. <https://doi.org/10.1002/2015JB012679>.
- Müller, R.D., Sdrolias, M., Gaina, C., Roest, W.R., 2008. Age, spreading rates, and spreading asymmetry of the world's ocean crust. *Geochem. Geophys. Geosyst.* 9 (4), 1525–2027. <https://doi.org/10.1029/2007GC001743>.
- Olyphant, T.E., 2007. Python for scientific computing. *Comput. Sci. Eng.* 9 (3), 10–20. <https://doi.org/10.1109/MCSE.2007.58>.
- Parsons, B., Sclater, J.G., 1977. An analysis of the variation of ocean floor bathymetry and heat flow with age. *J. Geophys. Res.* 82 (5), 803–827. <https://doi.org/10.1029/JB082i005p0803>.
- Perry, H.K.C., Forte, A.M., Eaton, D.W.S., 2003. Upper-mantle thermochemical structure below North America from seismic-geodynamic flow models. *Geophys. J. Int.* 154 (2), 279–299. <https://doi.org/10.1046/j.1365-246X.2003.01961.x>.
- Ricard, Y., Richards, M., Lithgow-Bertelloni, C., Le Stunff, Y., 1993. A geodynamic model of mantle density heterogeneity. *J. Geophys. Res., Solid Earth* 98 (B12), 21895–21909. <https://doi.org/10.1029/93JB02216>.
- Ritsema, J., van Heijst, H.J., Woodhouse, J.H., 2004. Global transition zone tomography. *J. Geophys. Res.* 109 (B2), B02302. <https://doi.org/10.1029/2003jb002610>.
- Sandwell, D.T., Smith, W.H.F., 2009. Global marine gravity from retracked Geosat and ERS-1 altimetry: ridge segmentation versus spreading rate. *J. Geophys. Res., Solid Earth* 114 (B1), B01411. <https://doi.org/10.1029/2008JB006008>.
- Schaeffer, A.J., Lebedev, S., 2013. Global shear speed structure of the upper mantle and transition zone. *Geophys. J. Int.* 194 (1), 417–449. <https://doi.org/10.1093/gji/ggt095>.
- Scheirer, D.S., Forsyth, D.W., Cormier, M.-H.I.n., Macdonald, K.C., 1998. Shipboard geophysical indications of asymmetry and melt production beneath the East Pacific Rise near the MELT experiment. *Science* 280 (5367), 1221–1224. <https://doi.org/10.1126/science.280.5367.1221>.
- Simmons, N.A., Forte, A.M., Boschi, L., Grand, S.P., 2010. GYPuM: a joint tomographic model of mantle density and seismic wave speeds. *J. Geophys. Res., Solid Earth* 115 (B12). <https://doi.org/10.1029/2010JB007631>.
- Spasojevic, S., Gurnis, M., 2012. Sea level and vertical motion of continents from dynamic Earth models since the Late Cretaceous. *Am. Assoc. Pet. Geol. Bull.* 96 (11), 2037–2064. <https://doi.org/10.1306/03261211121>.

- Stein, C.A., Stein, S., 1992. A model for the global variation in oceanic depth and heat flow with lithospheric age. *Nature* 359 (6391), 123–129.
- Steinberger, B., 2016. Topography caused by mantle density variations: observation-based estimates and models derived from tomography and lithosphere thickness. *Geophys. J. Int.* 205 (1), 604–621. <https://doi.org/10.1093/gji/ggw040>.
- Steinberger, B., Conrad, C.P., Osei Tutu, A., Hoggard, M.J., 2017. On the amplitude of dynamic topography at spherical harmonic degree two. *Tectonophysics*. <https://doi.org/10.1016/j.tecto.2017.11.032>.
- Sykes, T.J.S., 1996. A correction for sediment load upon the ocean floor: uniform versus varying sediment density estimations—implications for isostatic correction. *Mar. Geol.* 133 (1–2), 35–49. [https://doi.org/10.1016/0025-3227\(96\)00016-3](https://doi.org/10.1016/0025-3227(96)00016-3).
- Whittaker, J.M., Goncharov, A., Williams, S.E., Müller, R.D., Leitchenkov, G., 2013. Global sediment thickness data set updated for the Australian–Antarctic Southern Ocean. *Geochem. Geophys. Geosyst.* 14 (8), 3297–3305. <https://doi.org/10.1002/ggge.20181>.
- Yang, T., Moresi, L., Müller, R.D., Gurnis, M., 2017. Oceanic residual topography agrees with mantle flow predictions at long wavelengths. *Geophys. Res. Lett.* 44 (21), 10,896–810,906. <https://doi.org/10.1002/2017GL074800>.
- Zhong, S., Ritzwoller, M., Shapiro, N., Landuyt, W., Huang, J., Wessel, P., 2007. Bathymetry of the Pacific plate and its implications for thermal evolution of lithosphere and mantle dynamics. *J. Geophys. Res., Solid Earth* 112 (B6), B06412. <https://doi.org/10.1029/2006JB004628>.